Electronic Supporting Information

Resistive switching memories with enhanced durability enabled by mixed-dimensional perfluoroarene perovskite heterostructures

Michalis Loizos[1], Konstantinos Rogdakis[1,2*], Weifan Luo[3], Paul Zimmermann[4], Alexander Hinderhofer[4], Jovan Lukić[3], Marinos Tountas[1], Frank Schreiber[4], Jovana V. Milić[3*], and Emmanuel Kymakis[1,2*]

[1]Department of Electrical & Computer Engineering, Hellenic Mediterranean University (HMU), Heraklion 71410, Crete, Greece; [2]Institute of Emerging Technologies (i-EMERGE) of HMU Research Center, Heraklion; [3]Adolphe Merkle Institute, University of Fribourg, 1700 Fribourg, Switzerland; [4]Institute of Applied Physics, University of Tübingen, 72076 Tübingen, Germany. *Corresponding author e-mail: krogdakis@hmu.gr, jovana.milic@unifr.ch, kymakis@hmu.gr

Table of Contents

Experimental Section

Materials and methods

Commercially available materials chlorobenzene (CB, anhydrous, 98%), *N,N*-dimethylformamide (DMF, anhydrous, 99.8%), dimethyl sulfoxide (DMSO, anhydrous, ≥99.9%), toluene (anhydrous, 99.8%), cesium iodide (CsI, 99.999%, trace metals basis), rubidium iodide (RbI, 99.9%, trace metals basis), 2,9-dimethyl-4,7-diphenyl-1,10-phenanthroline (bathocuproine, BCP, 96%), were purchased from Sigma Aldrich. 2-Propanol (IPA, Extra Dry, 99.5%) was purchased from Acros Organics. Lead iodide (PbI_2, trace metals basis, 99.99%) and lead bromide ($PbBr_2$ >98.0%) were purchased from TCI. Formamidinium Iodide (FAI) and methylammonium bromide (MABr) were purchased from Dyenamo. Phenyl-C_{61}-butyric acid methyl ester ($PC_{61}BM$, 99%) was purchased from Solenne BV. Poly[bis(4-phenyl)(2,4,6-trimethylphenyl)amine] (PTAA, Mw = 20–70 kDa) was purchased from Solaris Chem. (*Perfluoro-1,4-phenylene)dimethylammonium iodide (F-PDMAI$_2$) and (perfluorobenzyl)ammonium ioidide (F-BNAI)* were synthesized and characterized based on the previously reported procedures.[1,2]

Thin film and device characterization

UV-vis absorbance spectra of thin films were recorded with a UV-2401 spectrophotometer from Shimadzu. Atomic Force Microscopy (AFM) images with 5 × 5 μm size were captured using an XE7 microscope from Park systems in tapping mode. *Water contact angle measurements* were performed with a L2004A1 goniometer from Ossila. *All electrical measurements* of the resistive switching memory devices, both in steady state and pulsed mode, were performed on a commercial ARKEO platform from Cicci Research s.r.l. Spring probes were attached to the top and bottom electrodes. The voltage was applied at the Ag top electrode, while the indium-doped tin oxide (ITO) bottom electrode was grounded. *Steady-state current-voltage characteristics of the memory devices* were measured by sweeping the voltage from 1.2V to -1V, with a scan rate of 100 mV s^{-1}. A compliance current of 10 mA was used to protect the devices. For pulsed measurements, a custom module by Cicci Research was developed. The module allows the custom design of waveform pulses. All measurements were performed in an ambient atmosphere (humidity 30–40%) at a controlled temperature of 25 °C under dark.

Grazing incidence wide-angle X-ray scattering (GIWAXS) was employed to analyze thin films deposited on microscope and ITO glass substrates at the SOLEIL synchrotron in France. The beam energy was 18.42 keV, the incidence angle 0–0.3°, and the beam size 60 × 50 µm. A Perkin Elmer XPAD140 detector with a spatial resolution of 130 µm was used to record two-dimensional diffraction patterns with a sample-to-detector-distance of 1182 mm. All measurements used an inert nitrogen atmosphere.

Device Fabrication

Glass/ITO substrates (Naranjo) were cleaned in sequence in water, acetone, and isopropyl alcohol ultrasonication bath for 10 min. The substrates were then dried in N_2 flow, following an oxygen plasma treatment for 5 min, and were then transferred to a N_2-filled glovebox for further processing. 2 mg ml^{-1} PTAA in toluene was spin-coated on the glass/ITO substrates at 6000 rpm for 30 s, and the substrates were then annealed at 100 °C for 10 min. The preparation of the perovskite precursor solution evolves from the preparation of a MAFA solution mixing by PbI_2, $PbBr_2$, FAI, and MABr in stoichiometric amounts, following the addition of RbI and CsI (1.5 M) from stock solutions. The final composition of the RbCsFAMA solution is $Rb_{0.04}Cs_{0.05}(FA_{0.85}MA_{0.15})_{0.91}Pb(I_{0.85}Br_{0.15})_3$. More details about the preparation of the perovskite solution can be found in previous reports by our group.[3] The perovskite precursor solution is then dynamically spin-coated at 6000 rpm for 45 s. 200 µl of chlorobenzene was then dropped on the center of the substrate 20 s before the end of the spinning process, and the samples were subsequently annealed at 100 °C for 45 min. Afterward, the PCBM solution in chlorobenzene with 20 mg ml^{-1} concentration was spin-coated on top of the perovskite layer at 2000 rpm for 60 s. The perfluoroarene solution (F-PDMAI or F-BNAI) at all concentrations (1, 2, 3, and 5 mg ml^{-1}) was prepared in IPA and was spin-coated on top of the perovskite layer at 3000 rpm for 30 s. The samples are then annealed at 100 °C for 5 min. BCP (0.5 mg ml^{-1} in IPA) is then dynamically spin-coated on the substrates. Finally, 100 nm Ag is thermally evaporated under a high vacuum (10^{-6} mbar) as the top electrode. The active area of the memory device is 4 mm^2.

Supplementary Data

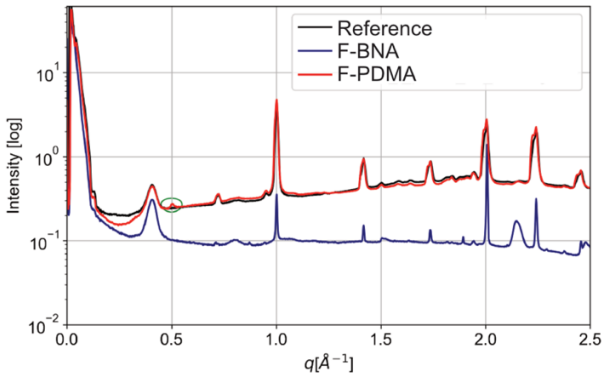

Figure S1. Radial profiles extracted from GIWAXS reciprocal space maps for reference (black), F-BNAI (blue, 1 mg ml^{-1}), and $F\text{-}PDMAI_2$ (red, 2 mg ml^{-1}) treated perovskite films. The $F\text{-}PDMAI_2$ system shows an additional peak at 0.5 Å at this concentration range, indicating the presence of the low-dimensional phase. Samples were measured at 0.14° incidence angle.

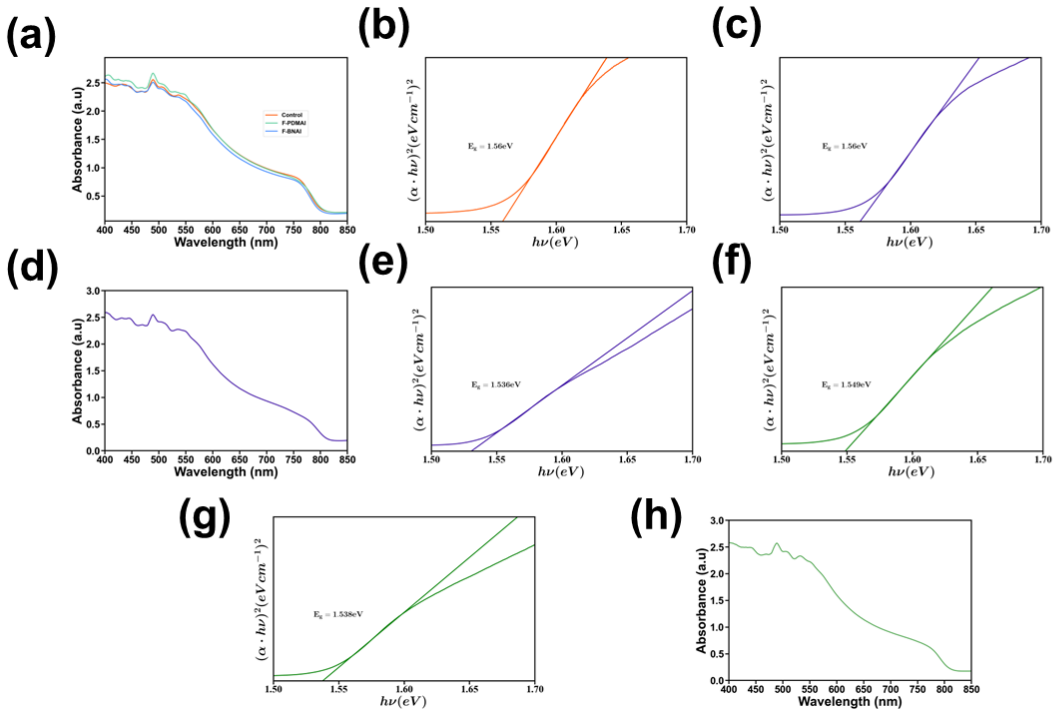

Figure S2. UV-vis absorption spectra of the (a) control, (d) F-BNAI and (h) F-PDMAI treated devices based on d) 5mg ml^{-1} F-BNAI and h) 5mg ml^{-1} F-PDMAI. Tauc plots of the b) control and c) 1mg ml^{-1} F-BNAI, e) 5mg ml^{-1} F-BNAI, f) 1mg ml^{-1} F-PDMAI, and g) 5mg ml^{-1} F-PDMAI treated devices.

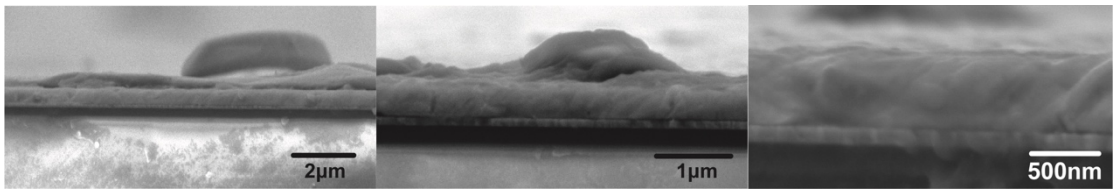

Figure S3. Cross-section SEM images of (a) control, (b) F-PDMAI$_2$-treated (2 mg ml^{-1}), and (c) F-BNAI-treated (1 mg ml^{-1}) perovskite devices.

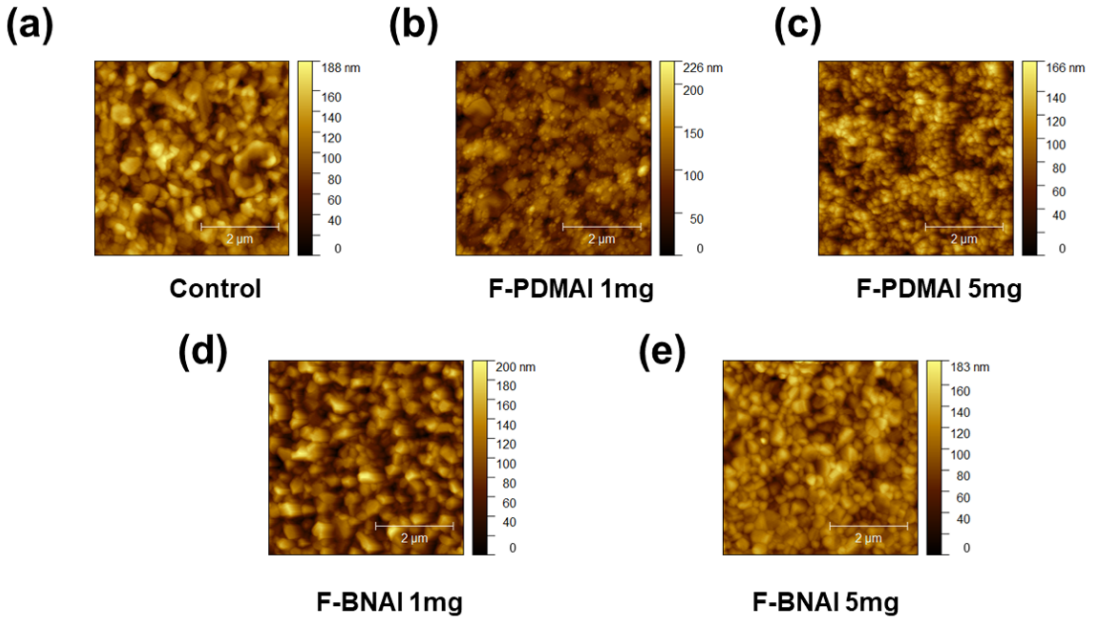

Figure S4. Atomic force microscopy images (5 μm × 5 μm) of perovskite films (a) without treatment and with (b) 1 mg ml^{-1} F-PDMAI$_2$, (c) 5 mg ml^{-1} F-PDMAI$_2$, (d) 1 mg ml^{-1} F-BNAI and (e) 5 mg ml^{-1} F-BNAI.

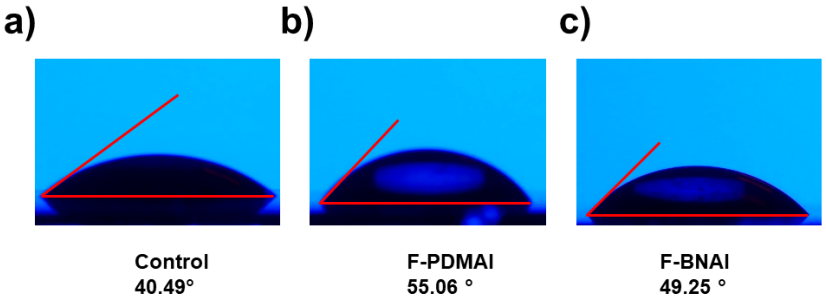

Figure S5. Contact angles of (a) control and (b–c) treated perovskite films with a water droplet.

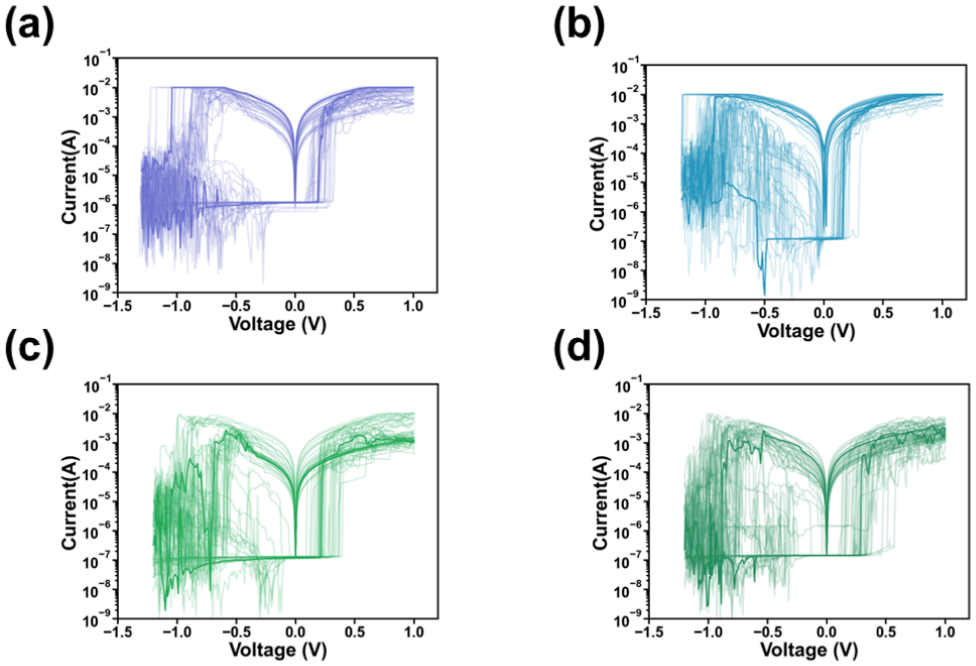

Figure S6. Current-voltage characteristics of 30 memory devices treated with (a) 2 mg ml^{-1} and (b) 3 mg ml^{-1} F-BNAI or (c) 1 mg ml^{-1} and (d) 3 mg ml^{-1} F-PDMAI$_2$. The optimal concentrations of 1 mg ml^{-1} for F-BNAI and 2 mg ml^{-1} F-PDMAI$_2$ are shown in the main article.

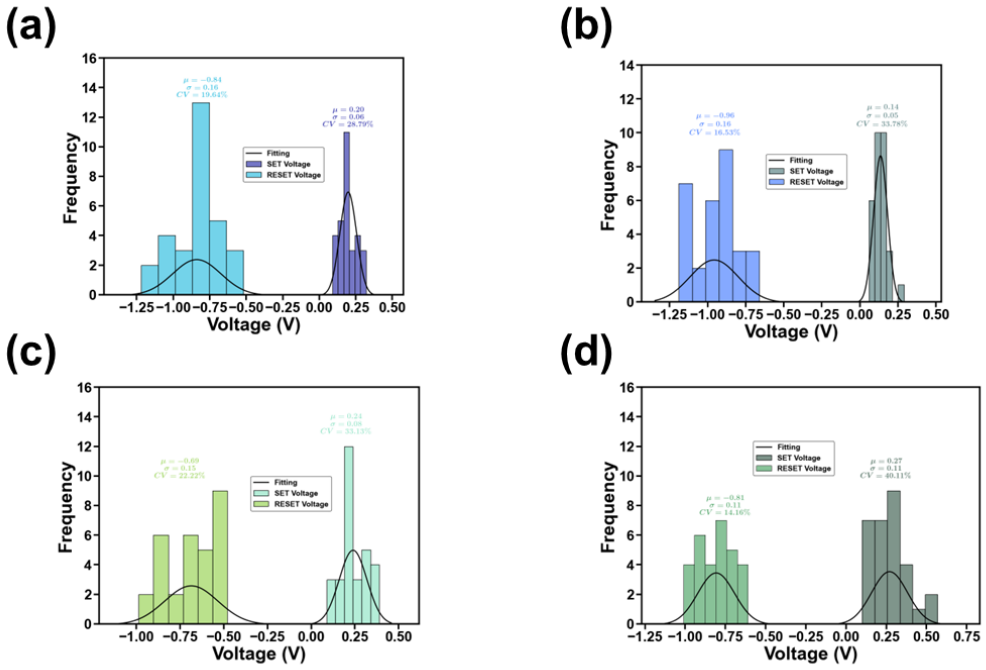

Figure S7. Switching voltage distribution of SET and RESET for memory devices treated with (a) 2 mg ml^{-1} F-BNAI, (b) 3 mg ml^{-1} F-BNAI, (c) 1 mg ml^{-1} F-PDMAI$_2$, and (d) 3 mg ml^{-1} F-PDMAI$_2$. The switching voltage distribution of SET and RESET for the optimal concentrations of 1 mg ml^{-1} for F-BNAI and 2 mg ml^{-1} F-PDMAI$_2$ are shown in the main manuscript.

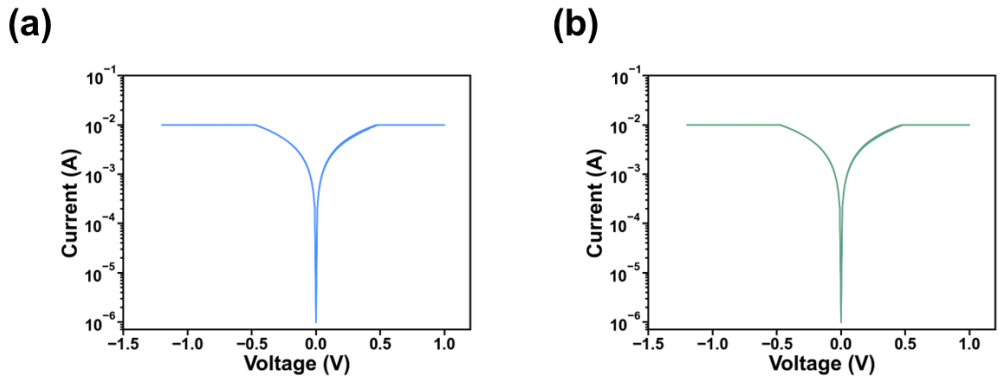

Figure S8. Current-voltage characteristics of the devices treated with (a) 5 mg ml^{-1} F-BNAI and (b) 5 mg ml^{-1} F-PDMAI$_2$.

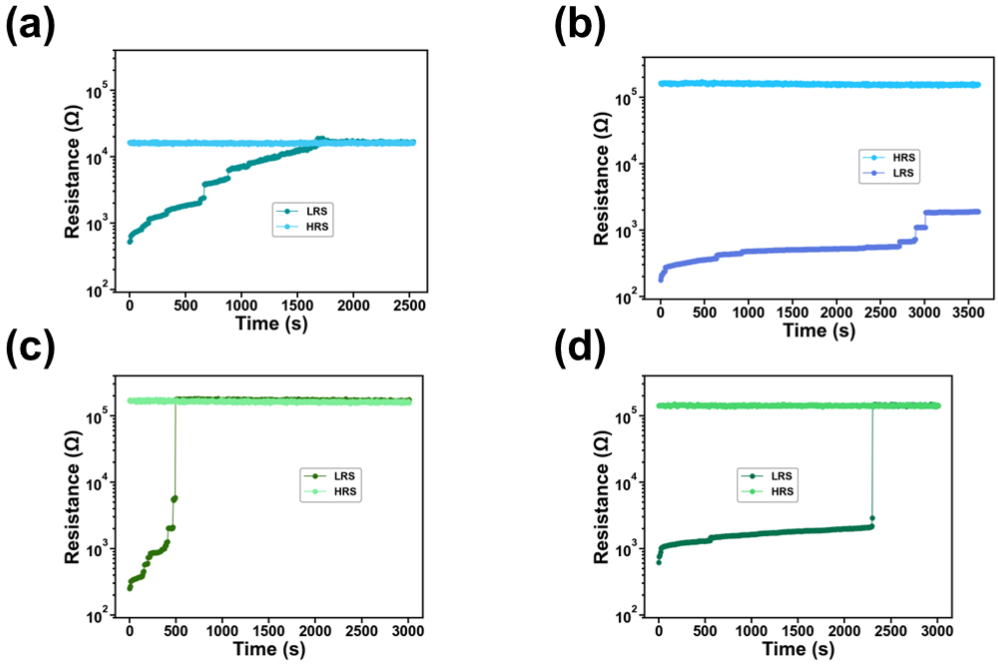

Figure S9. State retention of devices with (a) 2 mg ml^{-1} F-BNAI, (b) 3 mg ml^{-1} F-BNAI, (c) 1 mg ml^{-1}, and (d) 3 mg ml^{-1} F-PDMAI$_2$.

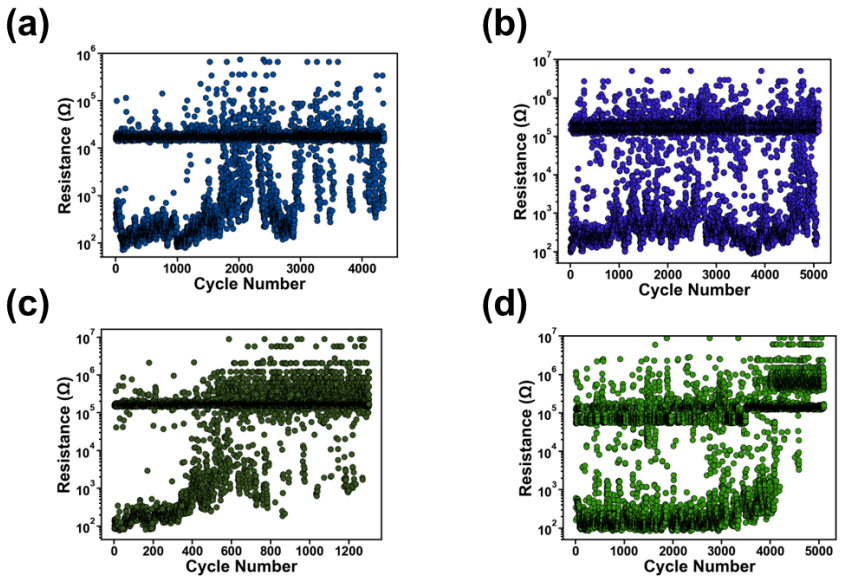

Figure S10. Cycling endurance of devices with (a) 2 mg ml^{-1} F-BNAI, (b) 3 mg ml^{-1} F-BNAI, (c) 1 mg ml^{-1} F-PDMAI$_2$ and (d) 3 mg ml^{-1} F-PDMAI$_2$. The endurance for the optimal concentrations of 1 mg ml^{-1} for F-BNAI and 2 mg ml^{-1} F-PDMAI$_2$ are shown in the main article.

Table S1. Average threshold switching voltage for SET and RESET process for control, F-PDMAI$_2$ and F-BNAI devices. The variation coefficient for each case is depicted in parentheses. All median and standard deviation values are obtained for 30 I-V sweeps.

Condition (concentration)	V_{SET} / V	V_{RESET} / V
Control	0.22±0.07 (34%)	-0.68±0.11 (16%)
F-PDMAI (1 mg)	0.24±0.08 (33%)	-0.69±0.15 (22%)
F-PDMAI (2 mg)	**0.17±0.04 (25%)**	**-0.68±0.06 (25%)**
F-PDMAI 3 mg	0.14±0.05 (34%)	-0.96±0.16 (16%)
F-BNAI 1 mg	**0.17±0.04 (22%)**	**-0.93±0.09 (10%)**
F-BNAI 2 mg	0.20±0.06 (29%)	-0.84±0.16 (20%)
F-BNAI 3 mg	0.14±0.05 (34%)	-0.96±0.16 (17%)

Table S2. Performance summary optimization for F-BNAI and F-PDMAI$_2$ memory devices. Optimised performances are highlighted in bold.

Condition (concentration)	Cycling Endurance [Cycles]	Retention [s]
Control	10^3	$1.2{\cdot}10^3$
F-PDMAI (1 mg)	$5{\times}10^2$	$5{\cdot}10^2$
F-PDMAI (2 mg)	$\mathbf{5{\times}10^3}$	$\mathbf{2.3{\cdot}10^3}$
F-PDMAI 3 mg	$4{\times}10^3$	$2.3{\cdot}10^3$
F-BNAI 1 mg	$\mathbf{10^4}$	$\mathbf{5{\cdot}10^3}$
F-BNAI 2 mg	$2.9{\times}10^3$	$3.6{\cdot}10^3$
F-BNAI 3 mg	$2.3{\times}10^3$	$1.2{\cdot}10^3$

Table S3. Performance comparison summary of various HP resistive switching devices.

Active Layer	Cycling Endurance [Cycles]	Retention [s]	Ref	Year
$MAPbI_3$	10^3	2.98×10^4	4	2017
$MAPbI_3$	10^3	10^4	5	2019
$MAPbI_{3-x}Cl_x$	10^4	2×10^3	6	2019
$Cs_{0.06}FA_{0.78}MA_{0.16}Pb(I_{0.92}Br_{0.08})_3$	10^3	10^5	7	2020
$FAPbI_3$ Nanocrystals	1.2×10^3	10^3	8	2020
en-doped $MAPbI_3$	1.2×10^4	10^5	9	2022
$FAPbI_3$	2×10^3	10^4	10	2023
$MAPbBr_3$	10^3	3×10^3	11	2024
This work (optimal performance)	10^4	5×10^3	-	2024

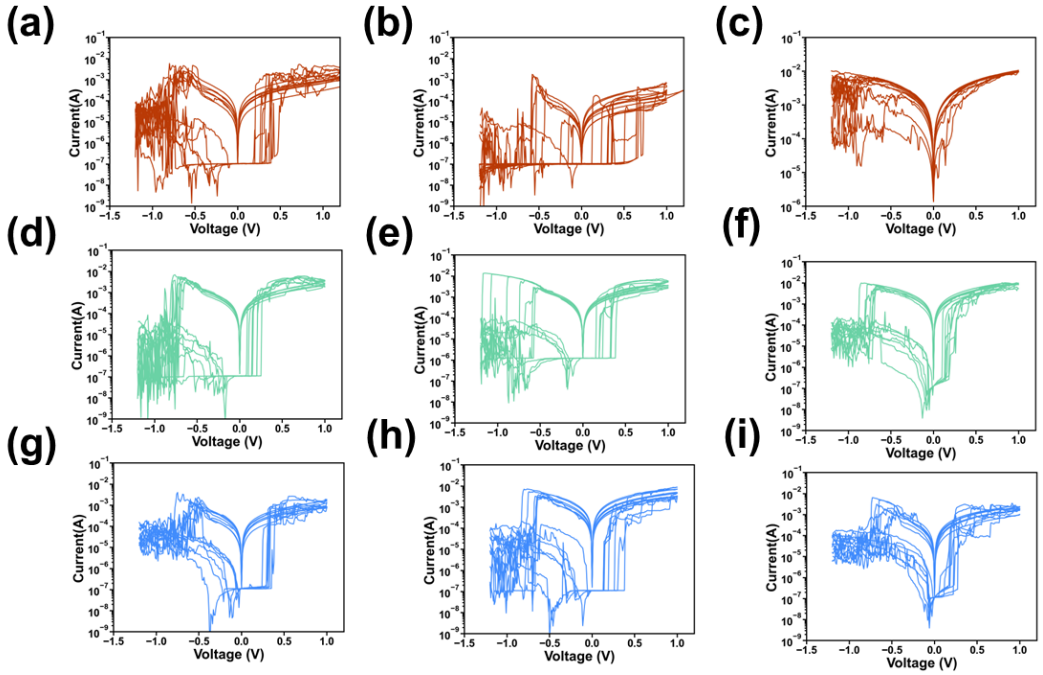

Figure S11. Current-voltage characteristics of the (a–c) control device after (a) 1 month, (b) 2 months, and (c) 3 months of storage in an inert N_2 atmosphere. Current-voltage characteristics of the optimal (d–f) F-$PDMAI_2$-treated and (g–i) F-BNAI-treated devices after (d,g) 1 month, (e,h) 2 months, and (f,i) 3 months of storage.

Table S4. Resistive switching parameter evolution of the control and optimal F-BNAI and F-$PDMAI_2$ treated memory devices for 3 months of storage in an inert nitrogen environment.

Inert Stability	1 Month			2 Months			3 Months		
Parameter	V_{SET} / V	V_{RESET} / V	ON/OFF	V_{SET} / V	V_{RESET} / V	ON/OFF	V_{SET} / V	V_{RESET} / V	ON/OFF
Control	0.27±0.06	-0.53±0.04	$2.95\cdot10^2$	0.42±0.20	-0.48±0.12	$8.2\cdot10^1$	Not operational		
F-BNAI	0.30±0.03	-0.60±0.08	$4.46\cdot10^2$	0.22±0.09	-0.68±0.06	$1.96\cdot10^3$	0.21±0.04	-0.77±0.07	$2.5\cdot10^3$
F-PDMAI	0.16±0.06	-0.71±0.04	1.01103	0.26±0.08	-0.79±0.23	$1.42\cdot10^2$	0.14±0.03	-0.71±0.07	$2.33\cdot10^3$

Table S5. Resistive switching parameter evolution of the control and optimal F-BNAI and F-$PDMAI_2$ memory devices for 40 days of exposure to ambient atmosphere.

	7 Days			10 Days			40 Days		
Parameter	V_{SET}/ V	V_{RESET}/ V	ON/OFF	V_{SET} / V	V_{RESET} / V	ON/OFF	V_{SET} / V	V_{RESET}/ V	ON/OFF
Control	0.13±0.02	-0.53±0.06	$3.82\cdot10^2$	0.34±0.23	-0.66±0.06	$4.17\cdot10^1$	0.26±0.13	-0.64±0.10	$3.27\cdot10^1$
F-BNAI	0.13±0.03	-0.88±0.13	$2.8\cdot10^3$	0.15±0.05	-0.84±0.09	$1.28\cdot10^2$	0.23±0.07	-0.97±0.05	$2.4\cdot10^2$
F-PDMAI	0.16±0.06	-0.62±0.02	$7.9\cdot10^2$	0.28±0.15	-0.55±0.06	$7.37\cdot10^1$	0.13±0.03	-0.80±0.08	$7.98\cdot10^1$

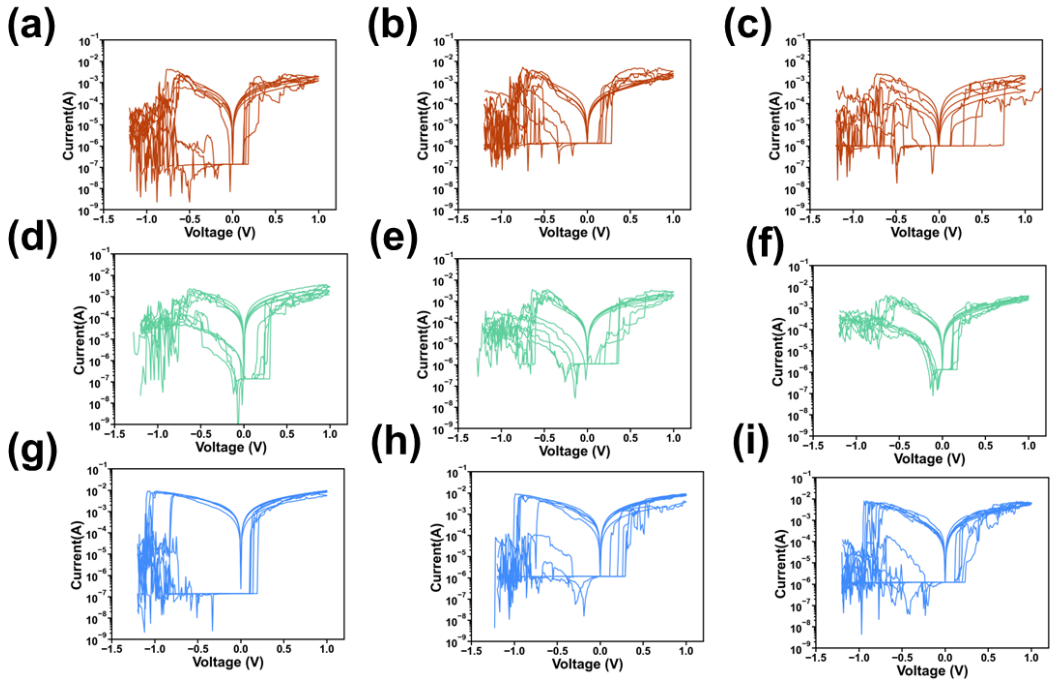

Figure S12. Current-voltage characteristics of (a–c) control and optimal (d–f) F-PDMAI$_2$ and (g–i) F-BNAI-treated devices after 7 (a,d,g), 10 (b,e,f), and 40 days (c,f,i) of exposure to air.

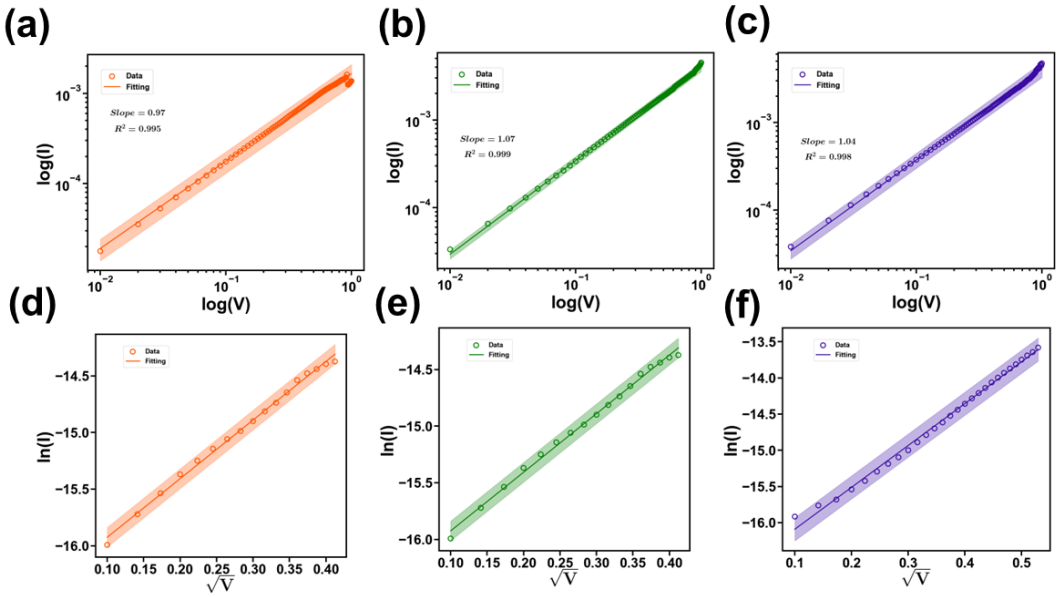

Figure S13. SCLC analysis at the (a–c) LRS and (d–f) HRS for the (a,d) control and optimal (b,e) F-PDMAI$_2$ and (c,f) F-BNAI treated devices.

References

1 M. Almalki, A. Dučinskas, L. C. Carbone, L. Pfeifer, L. Piveteau, W. Luo, E. Lim, P. A. Gaina, P. A. Schouwink, S. M. Zakeeruddin, J. V. Milić and M. Grätzel, *Nanoscale*, 2022, **14**, 6771–6776.

2 M. A. Hope, T. Nakamura, P. Ahlawat, A. Mishra, M. Cordova, F. Jahanbakhshi, M. Mladenović, R. Runjhun, L. Merten, A. Hinderhofer, B. I. Carlsen, D. J. Kubicki, R. Gershoni-Poranne, T. Schneeberger, L. C. Carbone, Y. Liu, S. M. Zakeeruddin, J. Lewinski, A. Hagfeldt, F. Schreiber, U. Rothlisberger, M. Grätzel, J. V. Milić and L. Emsley, *J. Am. Chem. Soc.*, 2021, **143**, 1529–1538.

3 K. Rogdakis, M. Loizos, G. Viskadouros, E. Kymakis, *Mater. Adv.* 2022, **3**, 7002.

4 J. Choi, Q. V. Le, K. Hong, C. W. Moon, J. S. Han, K. C. Kwon, P.-R. Cha, Y. Kwon, S. Y. Kim and H. W. Jang, *ACS Appl. Mater. Interfaces*, 2017, **9**, 30764–30771.

5 K. Kang, H. Ahn, Y. Song, W. Lee, J. Kim, Y. Kim, D. Yoo and T. Lee, *Adv. Mater.* 2019, **31**, 1804841.

6 A. Shaban, M. Joodaki, S. Mehregan and I. W. Rangelow, *Org. Electron.* 2019, **69**, 106–113.

7 Y. Huang, L. Tang, C. Wang, H. Fan, Z. Zhao, H. Wu, M. Xu, R. Shen, Y. Yang and J. Bian, *ACS Appl. Electron. Mater.*, 2020, **2**, 3695–3703.

8 C. Muthu, A. N. Resmi, J. K. Pious, G. Dayal, N. Krishna, K. B. Jinesh and C. Vijayakumar, *J. Mater. Chem. C*, 2021, **9**, 288–293.

9 K. Sakhatskyi, R. A. John, A. Guerrero, S. Tsarev, S. Sabisch, T. Das, G. J. Matt, S. Yakunin, I. Cherniukh, M. Kotyrba, Y. Berezovska, M. I. Bodnarchuk, S. Chakraborty, J. Bisquert and M. V. Kovalenko, *ACS Energy Lett.*, 2022, **7**, 3401–3414.

10 J.-H. Lee, J.-M. Yang, S.-Y. Kim, S. Baek, S. Lee, S.-J. Lee, N.-G. Park and J.-W. Lee, *Adv. Funct. Mater.* 2023, **33**, 2214142.

11 H. Kim, J. S. Kim, J. Choi, Y.-H. Kim, J. M. Suh, M.-J. Choi, Y.-S. Shim, S. Y. Kim, T.-W. Lee and H. W. Jang, *ACS Appl. Mater. Interfaces*, 2024, **16**, 2457–2466.